Geothermics 120 (2024) 102994

Contents lists available at ScienceDirect

Geothermics

journal homepage: www.elsevier.com/locate/geothermics

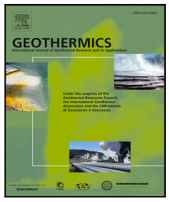

Source mechanism of kHz microseismic events recorded in multiple boreholes at the first EGS Collab testbed

Yan Qin [a], Jiaxuan Li [a], Lianjie Huang [a,*], Martin Schoenball [b], Jonathan Ajo-Franklin [b,c], Douglas Blankenship [d], Timothy J. Kneafsey [b], The EGS Collab Team

[a] Los Alamos National Laboratory, Los Alamos, 87545, NM, USA
[b] Lawrence Berkeley National Laboratory, 94720, CA, USA
[c] Rice University, Organization, Houston, 77005, TX, USA
[d] Sandia National Laboratories, Albuquerque, 87185, NM, USA

ARTICLE INFO

Dataset link: https://gdr.openei.org/egs_collab

MSC:
0000
1111

Keywords:
EGS Collab
High frequency (kHz)
Hydraulic fracturing
Microseismic monitoring
Moment tensor
Multiple boreholes
Stress state

ABSTRACT

Continuous microseismic monitoring using three-component (3C) accelerometers deployed in multiple boreholes allows for tracking the detailed evaluation of mesoscale (~10 m scale) fracture growth during the fracture stimulation experiments at the first Enhanced Geothermal Systems (EGS) Collab testbed. Building on a well-constrained microseismic event catalog, we invert for moment tensor of the events to better understand the fracture geometry and stress orientations. However, it is challenging because of the unknown orientation of 3C accelerometers and low signal-to-noise-ratio nature of high-frequency (several kHz) monitoring. To address these challenges, we first perform the hodogram analysis on the continuous active-source seismic monitoring (CASSM) data to determine the orientations of the 18 3C accelerometers. We then apply the principal component analysis (PCA) to the observed microseismic waveforms to improve the signal-to-noise ratios. We perform a grid search for the full moment tensor by fitting the PCA-denoised waveforms at a frequency range of 5 to 8 kHz. The moment tensor results show both the creation of hydraulic fractures and the reactivation of natural fractures during the hydraulic stimulations. Our stress inversion based on the inverted moment tensors reveals the alteration of stress regime caused by hydraulic fracture stimulations.

1. Introduction

The EGS Collab project performed a mesoscale (~10 m) field study of enhanced geothermal systems (EGS) at the Sanford Underground Research Facility (SURF) in Lead, South Dakota in 2018. The project conducted controlled, small-scale, in-situ EGS experiments on rock fracture behavior and permeability enhancement (Kneafsey et al., 2018). The goal of the project was to improve understanding of the relationship among stress, seismicity, and permeability enhancement during hydraulic stimulation. Experiment 1 of the EGS Collab testbed was located at the depth of 4850 ft and focused on hydraulic fractures through an integrated experimental and modeling effort. A wide range of geologic and geophysical data were collected and analyzed to characterize the changes with multiple stimulation and flow tests, including, active source seismic monitoring (Linneman et al., 2019; Chi et al., 2020; Gao et al., 2020), electrical resistance tomography (ERT) (Fu et al., 2018; Johnson et al., 2019), extended hydrologic characterization including tracer tests (Zhou et al., 2018; Mattson et al., 2019; Wu et al., 2021), distributed fiber optic sensors to monitor seismicity (DAS), temperature (DTS), and strain (DSS) changes (Fu et al., 2021), fracture aperture strain using the Step-rate Injection Method for Fracture In-situ Properties (SIMFIP) tool (Guglielmi et al., 2015b; Kneafsey et al., 2019), and passive microseismic monitoring (Schoenball et al., 2020; Chai et al., 2020; Fu et al., 2021).

Microseismic imaging is an essential tool to monitor the fracture initiation and propagation during fracture stimulations in EGS. The correlations between microseismicity and injection rate/pressure reflect the seismic response of a fracture zone (Warpinski, 2014). The event locations and moment tensors help delineate the fracture geometry (Fu et al., 2021) and fracturing mode (Eyre and van der Baan, 2015). Multiple studies have analyzed the seismic activities at mesoscale hydraulic fracturing and shear activation, which help bridge the gap between small-scale (cm) laboratory experiments and large-scale (km) observations. At Grimsel Test Site (GTS) underground rock laboratory in southern Switzerland, researchers (Gischig et al., 2018) analyzed microseismicity during mesoscale hydraulic fracturing and found that the microseismic events had double-couple sources but the tensile

* Corresponding author.
E-mail address: ljh@lanl.gov (L. Huang).

https://doi.org/10.1016/j.geothermics.2024.102994
Received 6 October 2023; Received in revised form 26 January 2024; Accepted 10 March 2024
Available online 19 March 2024

failure mechanism could not either be inferred or excluded. The study from Zang et al. (2017) reported different seismic responses during three different water injection schemes (continuous, progressive, and pulse injection) at the Äspö Hard Rock Laboratory, Sweden. Kwiatek et al. (2018) further performed moment tensor analysis on the events at the same site and found that the seismicity mainly occurred because of the reactivation of preexisting fractures with low values of isotropic components. At the Low Noise Underground Laboratory (France), high-pressure water was injected into limestone at 280 m depth at a 10-m scale, and studies showed that once a pressure threshold was reached, aseismic motions occurred and only a small fraction of energy was radiated as seismic events (Derode et al., 2015; Guglielmi et al., 2015a; Duboeuf et al., 2017).

For the EGS Collab experiment 1 testbed, passive seismic data have been analyzed from different aspects. Schoenball et al. (2020) processed the passive seismic data to obtain event locations and relative magnitudes. The location methods were tested on CASSM data, and the achieved location uncertainty was on the order of 1 m. By comparing the seismicity response to stimulation data, they found that the fracture network, including both hydraulic fractures and reactivated preexisting structures, was strongly influenced by rock fabric, preexisting fractures, and stress heterogeneities. Fu et al. (2021) identified four hydraulic fractures with high certainty by combining fracture-wellbore intersection observations from distributed temperature sensing (DTS), visual observations from an open-hole well, and prior in-situ stress measurements.

Based on the previous work on the EGS Collab project, we focus on the moment tensor inversion of the located microseismic events, which could help quantify the fracture geometry, the fracturing mode (shear vs tensile cracking), and the local stress regime. In this paper, we start with a brief description of the microseismic monitoring network, and then introduce the methods and workflow we use to obtain moment tensors. Next, we present the inverted moment tensor results by comparing them to mapped fracture planes and the injection history. In the discussion section, we compare our findings with other hydraulic fracturing sites and present inversion results of the local stress regime obtained using the inverted moment tensors.

2. Borehole microseismic monitoring network

The experiment 1 of EGS Collab is within a host rock consisting of carbonate-rich, quartz-bearing phyllite of the upper Poorman formation (Caddey, 1991). Over 450 m of core retrieved shows that natural fractures are prevalent in the testbed, including foliation, veining, bedding, fractures, and variations in mineralogy (Kneafsey et al., 2020). Microseismic monitoring utilizes a dense 3D borehole sensor array including 18 three-component (3C) piezoelectric accelerometers deployed in 6 monitoring boreholes (OB, OT, PDB, PDT, PSB, PST) (Fig. 1), surrounding the stimulation region (Schoenball et al., 2019a). Out of 18 accelerometers, only 12 of them are used for microseismic monitoring, and the temporal sampling frequency is 100 kHz. The borehole microseismic monitoring network is designed and optimized for microearthquake location and focal mechanism inversion in anisotropic media (Chen et al., 2019). Besides the six monitoring wells, an injection well (E1-I) and a production well (E1-P) are drilled approximately parallel to the minimum principal stress direction, which is oriented NS and plunges at an angle of approximately 9.3° (Dobson et al., 2018; Kneafsey et al., 2020; Oldenburg et al., 2020). Theoretically, the fracture propagation direction is normal to the minimum principal stress orientation, connecting injection and production well.

The project conducted twelve hydraulic fracture stimulations in May, June, July, and December 2018 (Schoenball et al., 2020). During the hydraulic stimulations from May 22 to 25, a hydraulic fracture was initiated from the notch cut at the 50-m depth in the well E1-I by a lower injection rate and propagated to the production well under higher injection rates. The located microseismic events were observed to propagate away from the injection well as the hydraulic fractures grew. On June 25, 2018, two short stimulations, approximately 4 min each, were conducted in well E1-P at a depth of 39 m, where a hydraulic fracture intersection had been identified. Another high-injection-rate stimulation was performed in well E1-I at the 50 m depth later on June 25, 2018. Two shallow stimulations at 39 m were conducted on July 19 and 20, 2018, which featured a low injection rate (0.4 L/min) and a high injection rate (1.5 L/min), respectively. Subsequently, three more stimulations were performed on December 7, 21, and 22, 2018, at a depth of 43 m in the injection well E1-I. The microseismic events triggered by those stimulations were analyzed and grouped into different clusters based on their spatial location. Within each cluster, a fracture plane was determined by fitting the microseismic event locations using linear regression. Five fracture planes were mapped from May and June 2018 events (Fu et al., 2021), and another four from July and December 2018 events using the same method (personal correspondence with Dr. Pengcheng Fu) (Fig. 1b).

The moment tensor inversion is overall challenging for the mesoscale fracturing. First, because of the high-frequency band of the observed microseismicity (3–20 kHz, Fig. 2), the waveforms can be easily distorted by small-scale heterogeneous, anisotropic velocity structures (Angus et al., 2014), and other unaccounted noises. Second, the polarity of the P phase can be ambiguous because of the cycle skipping in a high-frequency band (Virieux and Operto, 2009). Furthermore, the instrument response of the accelerometers used for microseismic monitoring is either unknown or complex. One study (Schoenball et al., 2020) measured the instrumental response curve of one accelerometer and found that it had an approximate flat response of 1 V/g below 5 kHz and became significantly nonlinear, with several resonance frequencies above 5 kHz. We have not found a study to invert for moment tensors without instrument response information at such a high-frequency range. However, the monitoring system at the first of EGS testbed has several advantages to help mitigate the difficulties. First, the azimuthal coverage of accelerometers is good, as we have 3C accelerometers deployed in multiple boreholes to monitor the fracture stimulation region. Second, the microseismic events have been well located with uncertainty on the order of 1 m (Chai et al., 2020; Schoenball et al., 2020). The microseismic events have better signal-to-noise ratio (SNR) at the higher frequency range (8 kHz to 15 kHz), while the instrument response becomes complex at higher frequencies (Schoenball et al., 2020). To balance the SNR and instrument response, we select the frequency range of 5 k to 8 k (Fig. 2) to filter the waveform. At this frequency range, since only the instrument response of the X component shows slightly increased sensitivity and Y and Z components are almost flat, we assume that the waveform shape and polarities are not significantly affected by instrument response. Also, in the misfit function, we apply PCA analysis to extract dominant information for P and S waves and normalize the data to fit the radiation pattern instead of the absolute magnitude. All these procedures help mitigate the influence of the instrument response.

3. Methods

3.1. Determination of 3C accelerometer orientations

For the accelerometers in the slanted monitoring boreholes, the positive directions of the x-components are documented to be parallel to the monitoring well and pointing away from the drift, while the remaining two components may rotate along the x-component during the deployment. Therefore, we first perform hodogram analysis to determine the orientations of the 3C accelerometers using continuous active source seismic monitoring (CASSM) data acquired in those monitoring wells for 17 piezoelectric active seismic sources (Fig. 1a, blue stars).

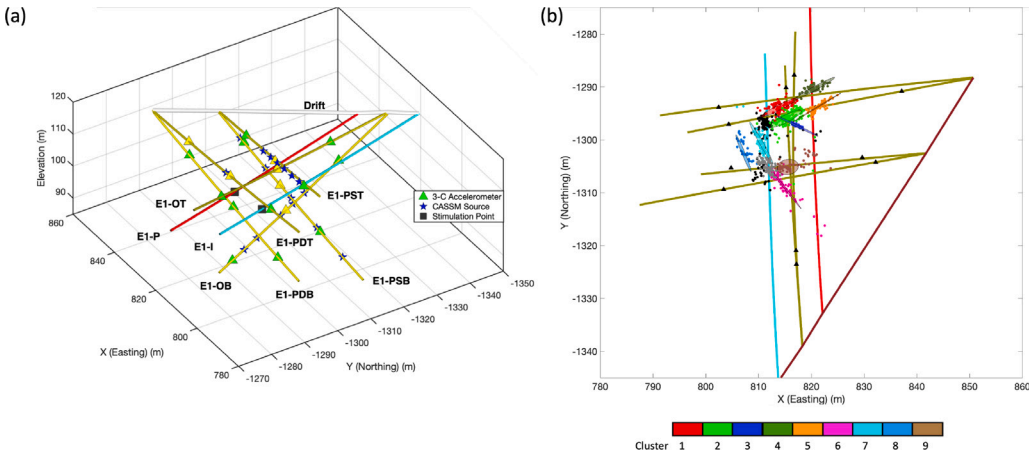

Fig. 1. (a) Borehole microseismic monitoring network at the first EGS Collab testbed. Cyan tube: the injection well (E1-I); red tube: the production well (E1-P). Yellow tubes: six monitoring wells with three 3C accelerometers (triangles) deployed in each of them. Twelve (green triangles) out of 18 accelerometers were used for microseismic monitoring. Blue stars: 17 CASSM sources. Black squares: stimulation locations at depth of about 50 m in E1-I and 39 m in E1-P. (b) Microseismic event location. 1067 microseismic events are divided into nine clusters denoted using different colors. The colored patches represent the fitted fracture planes using microseismic event locations (Fu et al., 2021). (For interpretation of the references to color in this figure legend, the reader is referred to the web version of this article.)

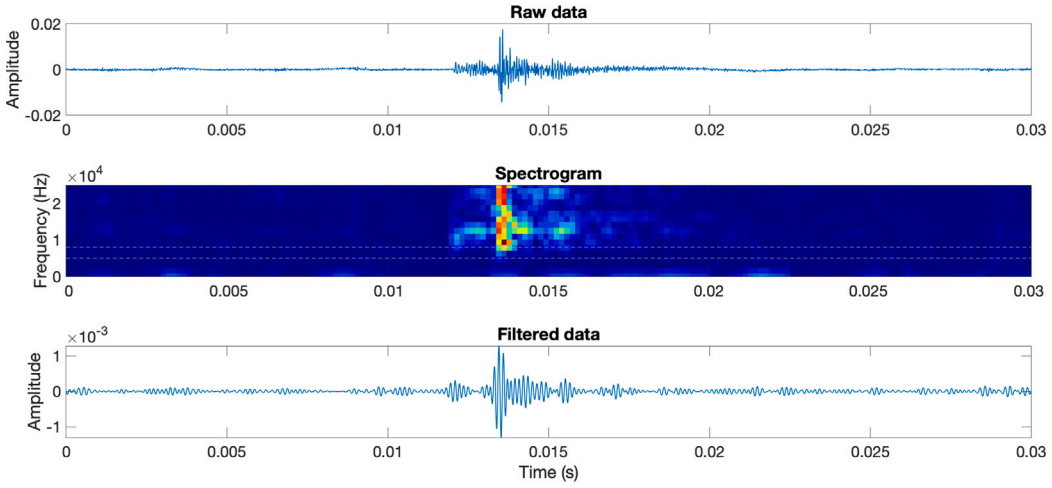

Fig. 2. Raw waveform, spectrogram, and filtered waveform for microseismic event at 2018-05-24T22:44:07 on fracture plane F1.

For each source–receiver pair recording, we rotate the waveform of y- and z-components, $y(t)$ and $z(t)$, by angle θ such that the energy for the P phase window $[t_b, t_e]$ in the y-component is minimized in the following objective function,

$$\min_{\theta} E(\theta) = \min_{\theta} \int_{t_b}^{t_e} [y(t)cos\theta - z(t)sin\theta]^2 dt. \tag{1}$$

When the energy of the P-phase window on the y-component is minimized, the rotated y-component $\vec{e}_{y\prime}$ should be perpendicular to the plane formed by the base vector of x-component $\vec{e}_x$ and the source–receiver vector $\vec{r}_{SR}$, that is, $\vec{e}_{y\prime}$ is the cross product between them: $\vec{e}_{y\prime} = \vec{e}_x \times \vec{r}_{SR}$. The true base vector of y-component $\vec{e}_y$ can be obtained by rotating the $\vec{e}_{y\prime}$ along the x-axis by angle $-\theta_{min}$ using the quaternion rotation.

For each accelerometer, we obtain 17 orientation results from 17 CASSM sources. To better constrain results, we select only source–receiver pairs with the angles between $\vec{r}_{SR}$ and $\vec{e}_x$ less than 20° to ensure the amplitudes on the y- and z-components are sufficiently large for the hodogram analysis. We then calculate the average rotation angle of the selected source–receiver pairs at each accelerometer. Finally, the average rotation angles are converted to the base vectors of three components defined in the East-North-Up (ENU) system (Table 1).

For each accelerometer, the recorded data $x(t)$, $y(t)$, and $z(t)$ can be converted from the local coordinate system to the ENU system $e(t)$, $n(t)$, and $u(t)$ using the following equation,

$$\begin{bmatrix} e(t) & n(t) & u(t) \end{bmatrix} = \begin{bmatrix} x(t) & y(t) & z(t) \end{bmatrix} * \begin{bmatrix} e_{x1} & e_{x2} & e_{x3} \\ e_{y1} & e_{y2} & e_{y3} \\ e_{z1} & e_{z2} & e_{z3} \end{bmatrix}. \tag{2}$$

3.2. Moment tensor inversion method

We develop a waveform-based moment tensor inversion method, which minimizes the misfit between the synthetic and the observed waveforms for both P- and S-phase windows. The synthetic displacement field of a point source can be calculated using (Aki and Richards, 2002),

$$u_k(\mathbf{r}, t) = G_{kp,q}(\mathbf{r}, t) m_{pq}, \tag{3}$$

where G is Green's function, m is moment tensor, and u is the displacement wavefield. $G_{kp,q}(\mathbf{r}, \mathbf{t})$ represents the kth component of the displacement for a single force along the pth direction at the source position. The subscript q represents the spatial derivative of Green's function along the qth direction. The synthetic source wavelet is a

Table 1
Base vectors of three components defined in ENU coordinate system for all the 18 borehole accelerometers.

Name	e_{x1}	e_{x2}	e_{x3}	e_{y1}	e_{y2}	e_{y3}	e_{z1}	e_{z2}	e_{z3}
PDT-1	−0.987	−0.132	−0.089	0.126	−0.302	−0.945	0.098	−0.944	0.314
PDT-2	−0.988	−0.124	−0.089	0.134	−0.431	−0.892	0.072	−0.894	0.443
PDB-3	−0.894	−0.012	−0.448	0.228	−0.873	−0.431	−0.386	−0.487	0.783
PDB-4	−0.898	−0.171	−0.405	0.438	−0.278	−0.855	0.034	−0.945	0.325
PDT-5	−0.990	−0.108	−0.088	0.059	0.246	−0.967	0.126	−0.963	−0.238
PDB-6	−0.892	−0.168	−0.419	0.430	−0.032	−0.902	0.138	−0.985	0.101
PSB-7	−0.906	−0.165	−0.388	0.374	0.114	−0.921	0.197	−0.980	−0.042
PSB-8	−0.903	−0.160	−0.400	−0.232	−0.602	0.764	−0.363	0.783	0.506
PSB-9	−0.898	−0.158	−0.411	0.212	−0.973	−0.091	−0.385	−0.169	0.907
PST-10	−0.994	−0.096	−0.057	0.092	−0.408	−0.908	0.064	−0.908	0.414
PST-11	−0.993	−0.096	−0.066	0.089	−0.257	−0.962	0.076	−0.962	0.263
PST-12	−0.993	−0.090	−0.072	−0.100	0.352	0.931	−0.058	0.932	−0.359
OB-13	−0.042	0.883	−0.467	0.292	−0.436	−0.851	−0.956	−0.173	−0.239
OB-14	−0.053	0.884	−0.465	−0.564	−0.411	−0.716	−0.824	0.225	0.520
OB-15	−0.060	0.883	−0.466	−0.884	−0.264	−0.387	−0.464	0.388	0.796
OT-16	0.023	0.988	−0.152	−0.701	0.125	0.703	0.713	0.090	0.695
OT-17	−0.009	0.990	−0.138	−0.944	−0.054	−0.324	−0.328	0.127	0.936
OT-18	−0.053	0.992	−0.113	−0.831	−0.107	−0.545	−0.553	0.065	0.830

modified cosine function (Ji et al., 2002). We test a range of source parameters and select a rise time of 5e-5 s for the best waveform fit. If we take the Voigt notation (Helnwein, 2001) to simplify the tensors by converting the 2D subscript (p, q) to 1D following (1, 1) → 1, (2, 2) → 2, (3, 3) → 3, (1, 2) = (2, 1) → 6, (1, 3) = (3, 1) → 5, (2, 3) = (3, 2) → 4, we can rewrite equation (3) as follows,

$$\begin{aligned} M_\alpha &= m_{pq}, \\ K_{k1} &= G_{k1,1}, \\ K_{k2} &= G_{k2,2}, \\ K_{k3} &= G_{k3,3}, \\ K_{k4} &= G_{k2,3} + G_{k3,2}, \\ K_{k5} &= G_{k1,3} + G_{k3,1}, \\ K_{k6} &= G_{k1,2} + G_{k2,1}, \\ \alpha &= 1...6, \\ p, q, k &= 1, 2, 3. \end{aligned} \tag{4}$$

The synthetic displacement field in Eq. (3) can then be rewritten as:

$$u_k(\mathbf{r}, t) = K_{k\alpha}(\mathbf{r}, t) M_\alpha. \tag{5}$$

Our goal is to minimize the energy of the difference between the observed seismograms d_k and synthetic data u_k as defined by $L(M_\alpha, \tau_\mathbf{r})$ the following equation by searching for the best-fit moment tensor parameters M_α and time shift $\tau_\mathbf{r}$ for each accelerometer,

$$L(M_\alpha, \tau_\mathbf{r}) = \sum_\mathbf{r} w_\mathbf{r} \int_{t_b}^{t_e} [d_k(\mathbf{r}, t + \tau_\mathbf{r}) - K_{k\alpha}(\mathbf{r}, t) M_\alpha]^2 dt, \tag{6}$$

where w_r is the weight for different receivers, which is the reciprocal of the source–receiver distance. Note that, in the modeling, the absolute amplitude is not well accounted for several reasons. First, we use non-viscous model and do not simulate the waveform attenuation. Then, we do not have information for sensor–borehole coupling and sensor instrument response at such high frequencies (kHz). In this study, we first normalize the observed waveform to synthetic waveform and then compute the misfit function, which honors the waveform phase fit and radiation pattern more than the absolute amplitude. Although the resulting scalar moment from the normalization could not represent the true absolute moment magnitude, it could still reveal the relative magnitudes among events.

3.3. Workflow

We first preprocess the waveform data, and then apply a multi-scale grid search method to invert for moment tensor parameters. We also apply quality control criteria to select the most reliable moment tensor results. Fig. 3 shows the workflow we use in this paper.

1. Preprocessing: First, we only select receivers with a source–receiver distance larger than 10 m to avoid the near-field effect. Then, we remove the mean and trend of the seismograms and apply a bandpass filter to seismic waveforms at a frequency band of 5–8 kHz. For each receiver, we rotate the data to locally radial, tangential, and transverse components and use principal component analysis to denoise the data (Vavryčuk et al., 2017). We select a 0.7 and 0.8 msec time windows for P phase (radial components) and S phase (tangential and transverse components), respectively. We weigh the P-phase window four times larger than the two S-phase windows in the misfit function. The length of the time window and the weight function are selected through trial and error to maximize the cross-correlation between the synthetic waveforms and the observed data.
2. Double couple (DC) moment tensor inversion: Assuming a constant velocity model (P wave velocity of 5900 m/s and v_p/v_s ratio of 1.78) (Schoenball et al., 2020), we apply a multi-scale grid search method to find the optimal DC parameters: strike, dip, and rake of the fault. In the initial coarse grid search, we use a grid interval of 5° and discard waveform segments with misfit error two times larger than the average misfit error and correlation coefficient lower than 0.35. This quality control iteration is terminated when no more updates are made to DC parameters. We then apply a finer grid search with a grid interval of 1° within 5° of the coarse-grid solution.
3. Non-double couple parameter inversion: We apply another multi-scale grid search for the two non-DC parameters ζ, and χ (Zhu and Ben-Zion, 2013; Zhu and Zhou, 2016). The strike, dip, and rake are constrained within 10° of the optimal pure DC solution. The grid interval for both parameters is 0.1 in the coarse grid search and 0.01 in the finer grid search. After obtaining the non-DC parameters, we calculate the isotropic (ISO) and compensated linear vector dipole (CLVD) components of the moment tensor following Vavryčuk (2015).
4. Quality control: To quantify the uncertainty of the results, we adopt the bootstrap resampling method to generate an ensemble of solutions. Then we use the following three criteria to select the most reliable results. First, the signal-to-noise ratio (SNR) of the event waveform should be larger than 2.0. Second, the waveform cross-correlation coefficient between synthetic and observation data should be larger than 0.6. Third, similar to Hardebeck and Shearer (2002, 2003), we require that the standard deviation of the angle difference between bootstrap resampling results and

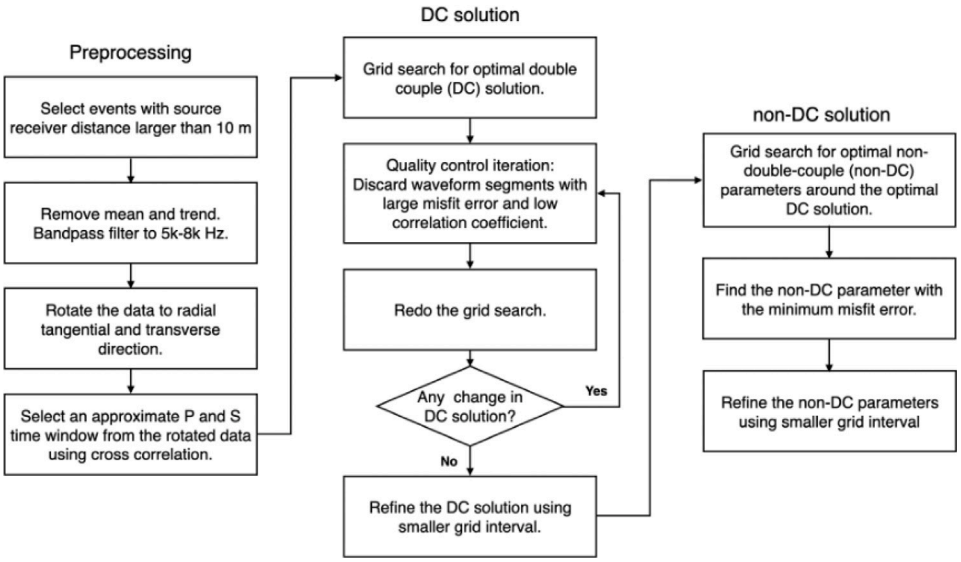

Fig. 3. Workflow for data preprocessing and moment tensor inversion of microseismic data.

results using all data be smaller than 20°. Starting with 1525 located events (Schoenball et al., 2020), we remove the events that are not temporally associated with stimulations or with high location uncertainty (25%) following Fu et al. (2021) and select 1067 events to compute moment tensors. After applying the above moment tensor selection criteria, we select 270 out of 1067 events to show in the next section.

4. Moment tensor inversion results

4.1. Double couple component

From May to December of 2018, hydraulic stimulations were conducted at three locations in the injection well E1-I at depths of 50.0 m, 39 m, and 43 m, respectively (see Schoenball et al. (2020) for detailed information). Over 1900 microseismic events were detected and located (Schoenball et al., 2020) and the cloud of microseismic events was interpreted as fracture planes based on their planar feature using linear-regression fitting (Fu et al., 2021). We present our moment tensor inversion results by comparing them with the fitted fracture planes in Fig. 4 and discuss the findings for each stimulation.

4.1.1. The stimulations at 50 m, May and June 2018

The first hydraulic stimulation test began on May 22, 2018, with an injection rate of 0.2 L/min and lasted over 10 min. The maximum injection pressure reached 26.0 MPa. During this period, 36 microseismic events were recorded and located within 3 m of the injection interval (Schoenball et al., 2020). On May 23, the stimulation continued at a flow rate of 0.4 L/min for 60 min with a maximum pressure of 26.8 MPa which enlarged the fracture to nominal diameter of 5 m. The seismicity grew in a planar fashion and formed the fracture plane F1. Fig. 4a shows inverted focal mechanism solutions along with the corresponding fitted fracture plane F1. The majority of inverted focal mechanism solutions show the dominant trend, although it is not fully aligned with the mapped fracture plane. The strikes of the inverted focal mechanisms are close to that of F1, but their dipping angles are systematically smaller.

On May 24, the injection rate increased to 5 L/min and lasted until fracture breakthrough into the production borehole (E1-P) was observed by downhole camera. The higher injection rate and maximum injection pressure of 27.3 MPa induced 280 events, forming a fracture plane F2 subparallel to F1. At the same time, fracture F3 with a strike of N120° E was also reactivated. The distribution of the moment tensor orientations on F2 is very similar to that on F1. The events on F3 that was identified as a natural fracture previously (Fu et al., 2021) show different orientations from those on F1 and F2 (Fig. 4c).

After an overnight shut-in, two stimulations with flow rate up to 4.5 L/min were conducted on May 25, 2018. A new fracture F4 formed during this stage. Seismicity continued for 30 min after the injection stopped. On F4, the strike of the moment tensors is aligned with the mapped fracture plane. Compared with F1, the events are dipping in the opposite direction (Fig. 4d). This observation of individual moment tensors is consistent with the overall seismicity cloud distribution, where the mapped F1 and F4 have similar strike but different dipping directions (Schoenball et al., 2020). The structural difference is possibly caused by the natural fracture plane that is located between F1 and F4.

On June 25, after one-month inactivity, the injection started in production well E1-P at a depth of 39 m where fracture breakthrough was detected previously. The injection rate was up to 4.3 L/min, the maximum injection pressure was 26.6 MPa, and 58 events occurred primarily on fracture plane F5 that intersects E1-P at the injection interval. Then the injection was switched back to injection well E1-I at 50 m at injection rate up to 4 L/min and injection pressure up to 35.1 MPa. During the first stage of injection from 19:00 to 19:30 in E1-I, only a few events occurred close to the injection well at the end where injection rate was increased, and we managed to obtain moment tensor for one event on F2. The injection ceased and resumed at 20:00, when more events occurred on F2 and F4. The lack of events during the first stage might be due to the relatively small injection rate and the delayed diffusion process. In the second stage, the microseismic events migrated away from the injection well (F2) to production well (F4). The moment tensors on F5 have the same distribution as F1 and F2. Fracture planes F1, F2, F4, and F5 have been identified as induced fractures in previous studies (Schoenball et al., 2020; Fu et al., 2021), and the consistent orientations of individual moment tensors (normal to the minimal principal stress orientation) support the statement.

4.1.2. The stimulations at 39 m, July 19 and 20, 2018

The shallowest stimulation was conducted at a depth of 39 m on July 19 and 20. The injection rates were 0.4 and 1.5 L/min, and the maximum injection pressure was 28.6 and 31.2 MPa, respectively. Fracture planes F7 and F8 were reactivated. The focal mechanisms on F7 show various orientations, and events on F8 have a dominant NS trend. Based on the orientations of fracture plane and individual focal mechanism solutions, we speculate that these fractures are reactivation of natural fractures instead of newly created hydraulic fractures.

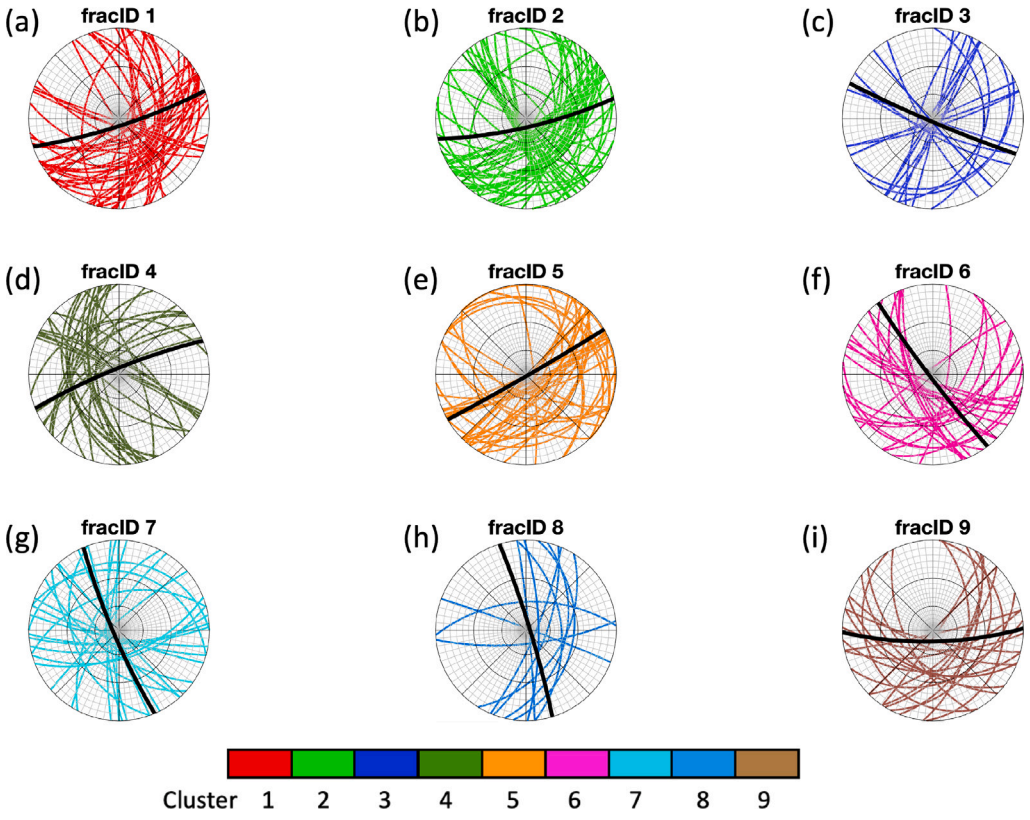

Fig. 4. Moment tensor DC inversion results for 270 selected events. Black thick lines represent the fitted fracture planes from microseismic event locations, and colorful thin lines represent the fault planes of moment tensor DC component for each cluster. The color scheme is the same as Fig. 1b. (For interpretation of the references to color in this figure legend, the reader is referred to the web version of this article.)

4.1.3. The stimulations at 43 m, December 2018

On December 7, 2018, the stimulation at 43-m depth in E1-I was conducted at a flow rate of 2.5 L/min and a maximum pressure of 33.7 MPa. On December 21 and 22, 2018, the flow rate was increased up to 5 L/min and the maximum pressure up to 35.2 MPa. Because of the high injection rate and injection pressure, 426 and 105 microseismic events were observed on December 21 and 22, respectively. Most events occurred on a new fracture plane F6, which grew from the injection interval to opposite directions of F7. A fracture plane F9 connecting injection and production was slowly formed during this stage. F9 has similar orientations as fracture planes F1, F2, F4, and F5 stimulated at 50 m depth. The orientation diversity of individual events within each cluster indicates that the fracture planes are not simple 2D planes but are composed of complex fabrics.

4.2. Non-double couple components

We also perform a full moment tensor inversion, and the waveform fit error is slightly smaller compared with DC moment tensor solutions. The results for each cluster are shown in the lune plot in Fig. 5. The lune plot shows the fracturing mode of each event, with pure DC component in the center, pure explosion/implosion (ISO) at top and bottom, and pure positive/negative CLVD source at left and right edges (Vavryčuk, 2015; Aso et al., 2016). The ISO and CLVD components typically exhibit either positive or negative values at the same time. Positive ISO and CLVD indicate a fracture opening caused by fluid injection, while negative ISO and CLVD represent a fracture closure. Most clusters show a combination of shear events and events with strong ISO and CLVD components in the source type diagram. Even though our intention is to create hydraulic fractures during experiment 1, a significant portion of shear events is observed, indicating the reactivation of natural fractures.

We further compare the CLVD component with the injection history in Fig. 6. Each subfigure represents a different stimulation stage in May, June, and December 2018. In each stage, we plot the CLVD components of microseismic events colored by the fracture planes with injection rate and pressure. At some specific stages and clusters, positive CLVD is associated with injection, and vice versa. For example, during the stimulation on May 25, 2018, the seismicity on fracture plane F4 lasted 30 min after injection shut-in, and the events show dominant negative CLVD (fracture closing) except for one. On June 25, 2018, most of the events on F5 show positive CLVD (fracture opening) during injection. However, overall, we observe "random" fracture opening and closing within each event cluster. A possible reason could be that the injection data is not measured at each event time and location; even the experiment scale is small, the diffusion process still can cause spatial and temporal delays in the seismicity response. In addition, not all mapped fractures are hydraulic fractures. The interactions among natural fractures, injection, and stress change can make the seismic response more complex.

5. Discussion

5.1. Moment tensor uncertainty characterization

To quantify the uncertainty of focal mechanism inversion results, we use three criteria to select events. As listed in the method section, the first criterion is that the signal-to-noise ratio (SNR) of the event waveform should be larger than 2.0. The second criterion is that the waveform cross-correlation coefficient between synthetic and observation data should be larger than 0.6. In Fig. 7, we show an example of

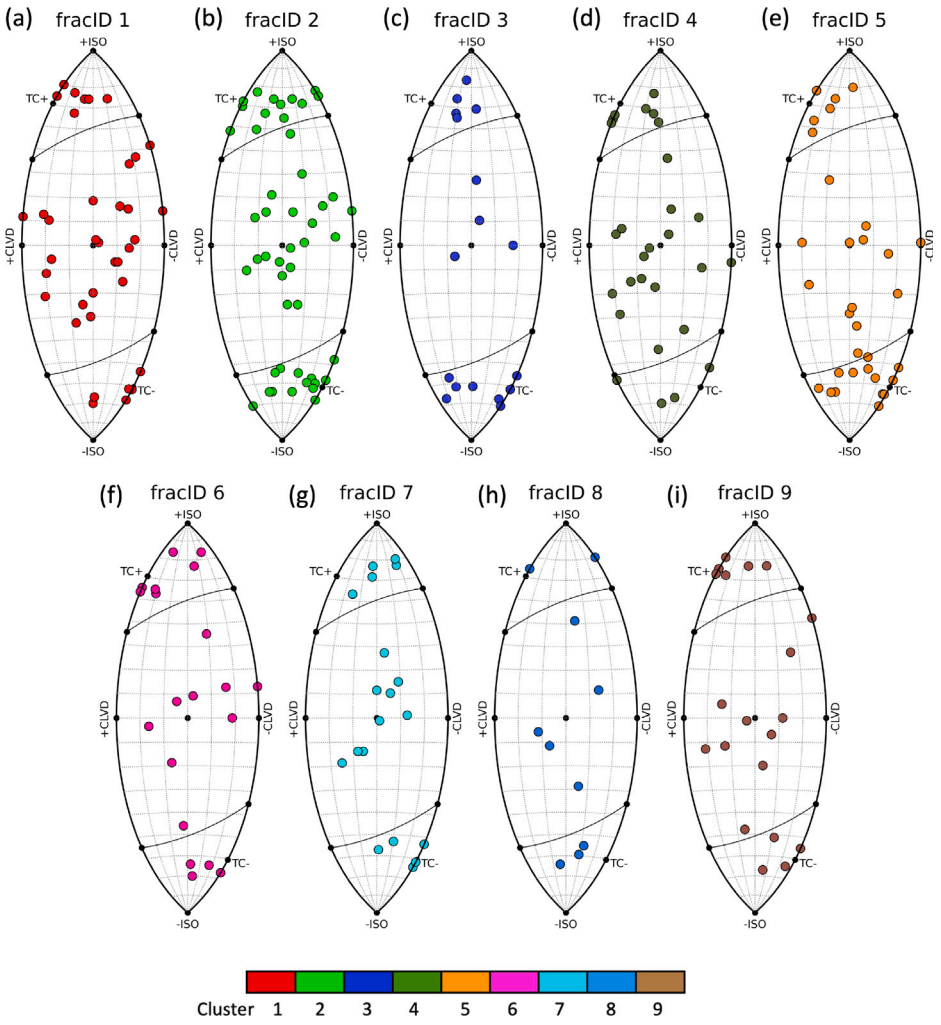

Fig. 5. (a) Source diagram lune plots for the 270 selected events. The Upper/lower corner represents a pure explosion/implosion source. The left/right side represents a pure positive/negative CLVD source. The center represents pure DC source. Colored dots represent the source diagram of individual microseismic events. The color scheme is the same as Fig. 1b. (For interpretation of the references to color in this figure legend, the reader is referred to the web version of this article.)

waveform fitting and the optimal DC solutions for one example event. The blue waveforms are discarded in the quality control iteration due to either large misfit error or low correlation coefficient. With PCA analysis, the cross-correlation coefficient is higher than those based on regular three-component waveform fitting. In Fig. 8a, we show the histogram of the number of segments used in the moment tensor inversion. On average, for each microseismic event, we use 78% of the available waveform segments (about 9 accelerometers), which can provide a good azimuth coverage. Fig. 8c shows the average correlation coefficients of used segments, and the mean value of correlation between observed and synthetic is about 0.68.

In the third criterion, we compare the angle difference between best-fit solutions with those from bootstrap resampling, and the standard deviations of the angle difference are defined as uncertainty. As shown in Fig. 8b, the average uncertainty of the selected events is 14°, suggesting that the DC solutions are relatively stable during bootstrap. Although we could not determine the absolute moment magnitude of each single event, we could compare the relative moment magnitudes among different events. In Fig. 8d, we show the cross plot between the average correlation coefficient with the relative scalar moment (normalized by the maximum scalar moment among all events). We find that when the relative magnitude is larger, the average correlation is higher, which is consistent with the observation that larger events have better signal-to-noise ratios.

5.2. Shear events

One of the most interesting findings in our work is the significant portion of shear events based on moment tensor inversion. The existence of shear events is supported by multiple independent datasets at experiment 1 of EGS Collab. First, SIMFIP tools (Guglielmi et al., 2015b) are installed in injection and production boreholes to monitor the relative three-dimensional displacement between two inflatable packers under high pressure fluid injections. Shear events are observed directly from SIMFIP monitoring (Schoenball et al., 2019b; Hopp et al., 2020; Schoenball et al., 2021). Second, the study of core samples reveals that natural fractures are prevalent in the testbed, including foliation, veining, bedding, fractures, and variations in mineralogy (Kneafsey et al., 2020). Lab experiments on the Poorman Schist sample show that the south-east striking with approximately 60° dip foliation planes (Frash et al., 2019a) are relatively weaker and can be reactivated by fluid injection under the pressure smaller than the minimal principal stress magnitude (as low as 6 MPa (Frash et al., 2019a)) (Frash et al., 2019b; Condon et al., 2020; Ye et al., 2020). Third, electrical resistivity tomography (ERT) inversion results show a highly heterogeneous rock fabric (Johnson et al., 2019). A lower seismic velocity region from depths of 45 m to 60 m is identified in the baseline data and shows high change in conductivity during injection, indicating the existence of the fractured zone (Linneman et al., 2019).

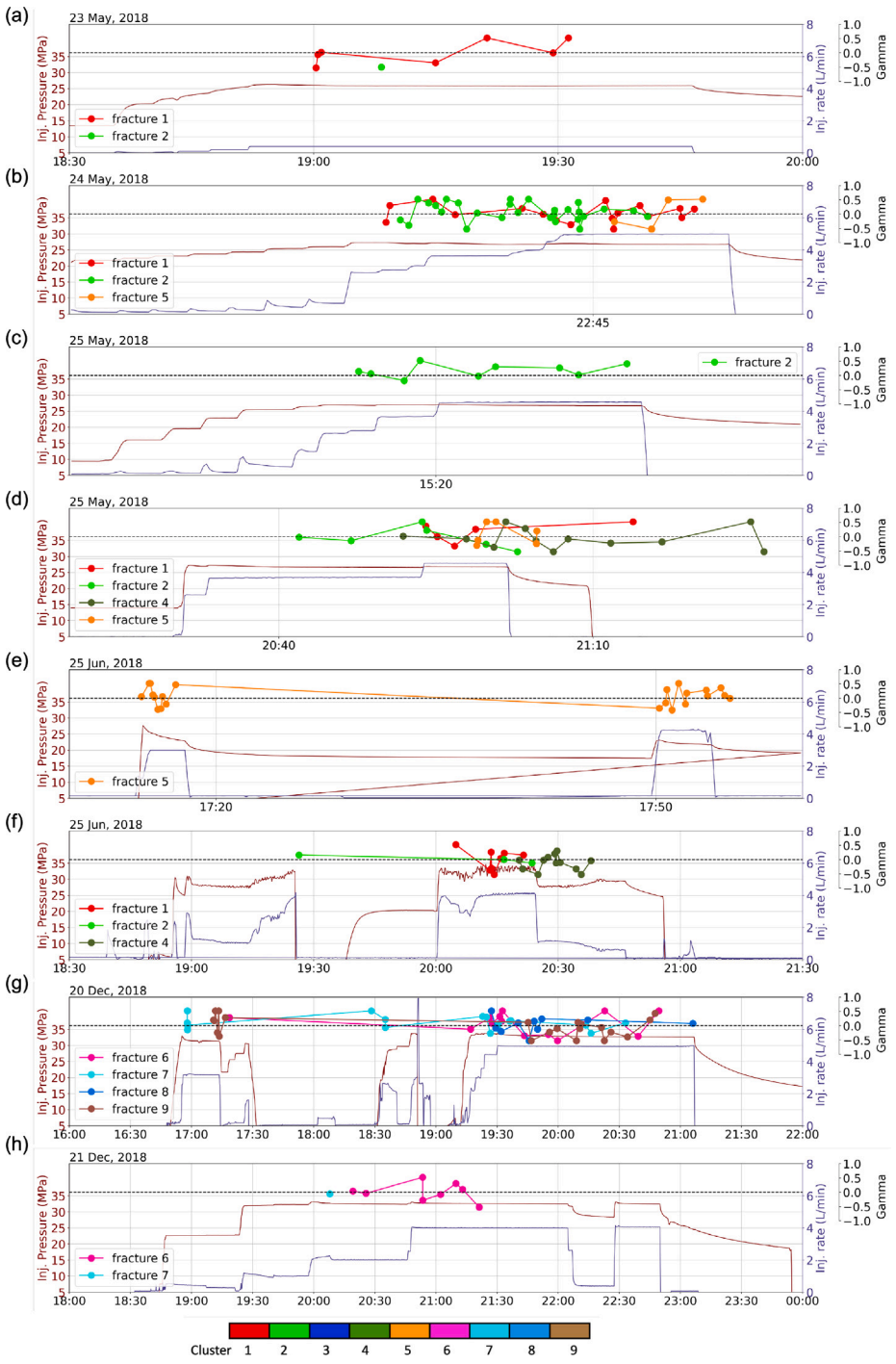

Fig. 6. Comparison of CLVD component of moment tensors and injection history. The brown and blue lines represent the injection pressure and injection rate, respectively. The colored dots are CLVD component of moment tensors from each cluster. The color scheme is the same as Fig. 1b. (For interpretation of the references to color in this figure legend, the reader is referred to the web version of this article.)

Although the primary mechanism is thought to be tensile fracturing, double couple mechanisms have been observed at multiple hydraulic fracturing sites (Ishida, 2001; Chitrala et al., 2013; Kwiatek et al., 2018; Gischig et al., 2018). Moment tensor analysis has shown that most induced events have a predominant double couple mechanism with only few having strong tensile component (Šílenỳ et al., 2009; Martínez-Garzón et al., 2017). The observation of dominant shear mechanism of hydraulic fracturing has been explained by fluid leak-off into small existing fractures (Dusseault et al., 2011), where the leak-off fluid increases the pore pressure, reduces the normal stress, and then promotes slip on the existing fractures. We notice that the mapped fracture planes F3, F6, F7, and F8 have different strike orientations from the theoretical hydraulic fracture orientation but consistent strike with the foliation planes, suggesting reactivation of pre-existing natural fractures.

5.3. Stress inversion

Based on the inverted moment tensors, we use the MSATSI software package (Martínez-Garzón et al., 2014) to invert for the local stress field. To obtain reliable principal stress orientations, the program requires a minimum of 20 focal mechanisms at each grid point. Stress

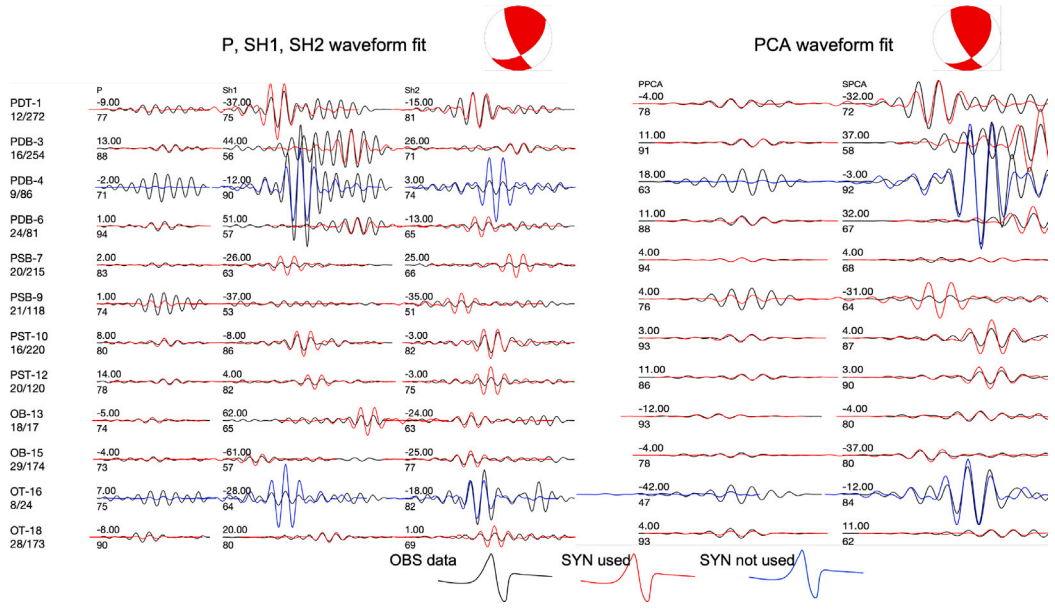

Fig. 7. An examples of waveform fitting of synthetic data and observed data for event at 2018-05-24T22:44:07 on fracture plane F1. The P-SH1-SH2 three-component waveform fit is shown on the left and PCA waveform fit on the right. Black waveforms are observation data. Red and blue waveforms are synthetic data used and not used in the inversion, respectively. The amount of shift (in data points) is marked on top of each segment, and the correlation coefficients are marked at the bottom. The beach balls show the best-fit DC solution. (For interpretation of the references to color in this figure legend, the reader is referred to the web version of this article.)

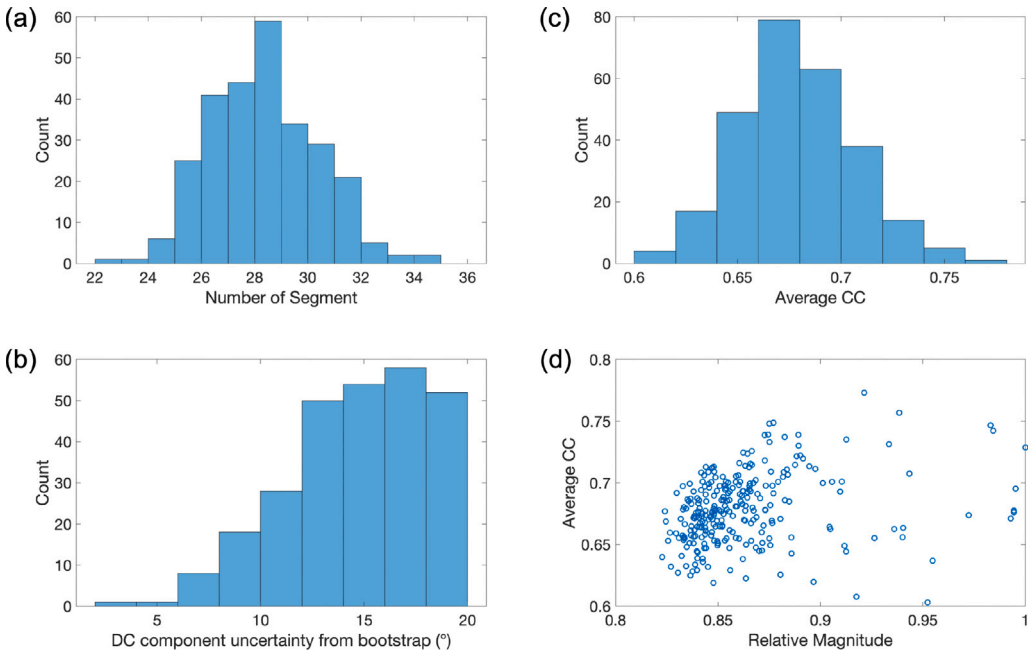

Fig. 8. (a) Histogram of the number of segments used in the inversion for the selected 270 events. Since we are using twelve 3C accelerometers, the number of available segments is 36. (b) Histogram of the average correlation coefficient of the segments used in the inversion. (c) Histogram of the DC component uncertainty, which is defined as the standard deviation of the angle difference between best-fit focal mechanism solutions and bootstrap resampling results. (d) Cross plot of the relative magnitude (normalized to 1) with the average correlation coefficient.

measurements conducted adjacent to the Experiment 1 site reveal that the minimum horizontal stress σ_{hmin} is about 21.7 MPa and trends approximately NS with a slight plunge of 9.3° to the NNW. At the depth of ~1530 m, the vertical stress σ_v magnitude is around 41.8 MPa, and the maximum horizontal stress σ_{Hmax} is estimated to be 34.0 MPa (Dobson et al., 2018; Kneafsey et al., 2020; Oldenburg et al., 2020). Since $\sigma_v > \sigma_{Hmax} > \sigma_{hmin}$, the experiment 1 testbed is in a normal faulting regime with σ_{Hmax} trending EW.

Fig. 9 shows the stress inversion results derived from the moment tensors of the microseismic events. First, the results show that all clusters are in either a normal faulting or oblique normal faulting regime. This is consistent with previous observations that the relative magnitudes of principal stresses vary with depth, and at a depth of 1550 m $\sigma_v \approx \sigma_{Hmax} > \sigma_{hmin}$ in the West Access Drift (Wang et al., 2017). However, the σ_{Hmax} orientations show large variations from the background stress state before stimulation. Between the injection well and production well, for cluster 1, 2, 3, 4, and 5, the σ_{Hmax} orientations rotate from EW to NE direction, and the σ_{Hmax} orientation of cluster 6 rotates to SE direction. To the west of the injection well, the σ_{Hmax} orientations for cluster 7, 8, and non-clustered events (black

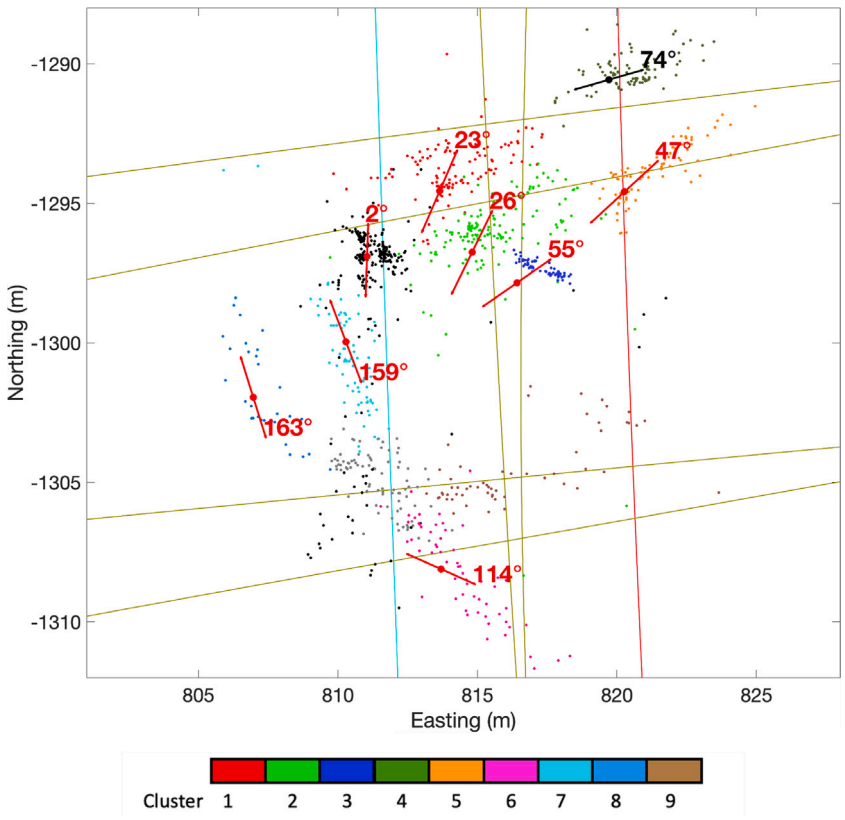

Fig. 9. Maximum principal horizontal stress orientations inverted from moment tensors in each cluster. The red and black bars represent normal and oblique normal faulting regime, respectively. The numbers next to the bars are the orientation angles. The colored dots are microseismic events in different clusters. The plotting scheme is the same as Fig. 1b. (For interpretation of the references to color in this figure legend, the reader is referred to the web version of this article.)

dots) rotate to NS direction. The heterogeneity of the stress state could be attributed to several factors. First, previous studies have shown that boreholes act as stress relief points, arresting fracture growth in EGS Collab experiment 1 (Frash et al., 2018, 2019a, 2020; Schoenball et al., 2020). The heterogeneous stress field possibly reflects local stress alterations caused by stimulations and boreholes. Second, anisotropy of the velocity model could also impact the moment tensor inversion and stress inversion results. For example, the natural discontinuities, like foliation, could introduce anisotropy and deviate the orientation of the hydraulic fractures from the normal of the minimal principal stress (Gischig et al., 2018). Based on the active seismic survey data, the testbed has showed a significantly high level of seismic anisotropy, with Thomsen parameters of ϵ, δ, and γ up to 0.6, 0.4, and 0.4, respectively (Gao et al., 2020).

6. Conclusions

We have determined the orientations of the three-component accelerometers using hodogram analysis of 17 CASSM shot data acquired at the first EGS Collab testbed. We have employed the principal component analysis of the observed microseismic waveforms to improve the signal-to-noise ratios. After orientation correction, we have inverted for the full moment tensor for the cataloged events using a two-step multi-scale grid search method. The moment tensor results show both events with large isotropic (ISO)/compensated linear vector dipole (CLVD) components and events with large double couple (DC) components, indicating the creation of hydraulic fractures and reactivation of natural fractures, respectively. The stress inversion results reflect the heterogeneous stress state alterations caused by stimulations. Interactions among fluid flow, pore pressure, stress, and anisotropy result in complex seismic response during the hydraulic stimulations of the EGS Collab experiment 1.

CRediT authorship contribution statement

Yan Qin: Data curation, Formal analysis, Investigation, Methodology, Software, Writing – original draft, Writing – review & editing. **Jiaxuan Li:** Data curation, Formal analysis, Investigation, Methodology, Software, Writing – original draft, Writing – review & editing. **Lianjie Huang:** Conceptualization, Formal analysis, Funding acquisition, Investigation, Methodology, Project administration, Resources, Supervision, Writing – original draft, Writing – review & editing. **Martin Schoenball:** Data curation. **Jonathan Ajo-Franklin:** Data curation, Writing – review & editing. **Douglas Blankenship:** Conceptualization, Project administration, Funding acquisition. **Timothy J. Kneafsey:** Conceptualization, Funding acquisition, Project administration.

Declaration of competing interest

The authors declare that they have no known competing financial interests or personal relationships that could have appeared to influence the work reported in this paper.

Data availability

The data are open to public at https://gdr.openei.org/egs_collab.

Acknowledgments

This material was based upon work supported by the U.S. Department of Energy (DOE), Office of Energy Efficiency and Renewable Energy (EERE), Office of Technology Development, Geothermal Technologies Office, under Contract No. 89233218CNA000001 to Los Alamos National Laboratory (LANL). LANL is operated by Triad National Security, LLC, for the National Nuclear Security Administration

(NNSA) of U.S. DOE. This research used resources provided by the LANL Institutional Computing Program, which is supported by the U.S. DOE NNSA under Contract No. 89233218CNA000001. The United States Government retains, and the publisher, by accepting the article for publication, acknowledges that the United States Government retains a non-exclusive, paid-up, irrevocable, world-wide license to publish or reproduce the published form of this manuscript, or allow others to do so, for United States Government purposes. The research supporting this work took place in whole or in part at the Sanford Underground Research Facility in Lead, South Dakota. The assistance of the Sanford Underground Research Facility and its personnel in providing physical access and general logistical and technical support is acknowledged. We thank Dr. Pengcheng Fu for his insightful discussions. All the data used in this work are open data available at https://gdr.openei.org/egs_collab.

EGS Collab Team: J. Ajo-Franklin, T. Baumgartner, K. Beckers, D. Blankenship, A. Bonneville, L. Boyd, S. Brown, J.A. Burghardt, C. Chai, T. Chen, Y. Chen, K. Condon, P.J. Cook, D. Crandall, P.F. Dobson, T. Doe, C.A. Doughty, D. Elsworth, J. Feldman, A. Foris, L.P. Frash, Z. Frone, P. Fu, K. Gao, A. Ghassemi, Y. Guglielmi, B. Haimson, A. Hawkins, J. Heise, M. Horn, R.N. Horne, J. Horner, M. Hu, H. Huang, L. Huang, K.J. Im, M. Ingraham, R.S. Jayne, T.C. Johnson, B. Johnston, S. Karra, K. Kim, D.K. King, T. Kneafsey, H. Knox, J. Knox, D. Kumar, K. Kutun, M. Lee, D. Li, J. Li, K. Li, Z. Li, M. Maceira, P. Mackey, N. Makedonska, C.J. Marone, E. Mattson, M.W. McClure, J. McLennan, T. McLing, C. Medler, R.J. Mellors, E. Metcalfe, J. Miskimins, J. Moore, J.P. Morris, S. Nakagawa, G. Neupane, G. Newman, A. Nieto, C.M. Oldenburg, W. Pan, T. Paronish, R. Pawar, P. Petrov, B. Pietzyk, R. Podgorney, Y. Polsky, J. Pope, S. Porse, Y. Qin, B.Q. Roberts, M. Robertson, W. Roggenthen, J. Rutqvist, D. Rynders, M. Schoenball, P. Schwering, V. Sesetty, A. Singh, M.M. Smith, H. Sone, F.A. Soom, P. Sprinkle, C.E. Strickland, J. Su, D. Templeton, J.N. Thomle, C. Ulrich, N. Uzunlar, A. Vachaparampil, C.A. Valladao, W. Vandermeer, G. Vandine, D. Vardiman, V.R. Vermeul, H.F. Wang, J. Weers, N. Welch, M.D. White, P. Winterfeld, T. Wood, S. Workman, H. Wu, Y.S. Wu, E.C. Yildirim, Y. Zhang, Y.Q. Zhang, Q. Zhou, M.D. Zoback

References

Aki, K., Richards, P.G., 2002. Quantitative seismology.

Angus, D., Aljaafari, A., Usher, P., Verdon, J., 2014. Seismic waveforms and velocity model heterogeneity: towards a full-waveform microseismic location algorithm. J. Appl. Geophys. 111, 228–233.

Aso, N., Ohta, K., Ide, S., 2016. Mathematical review on source-type diagrams. Earth Planets Space 68, 1–21.

Caddey, S.W., 1991. The Homestake gold mine, an early Proterozoic iron-formation-hosted gold deposit, Lawrence County, South Dakota, No. 1857. US Government Printing Office.

Chai, C., Maceira, M., Santos-Villalobos, H.J., Venkatakrishnan, S.V., Schoenball, M., Zhu, W., Beroza, G.C., Thurber, C., EGS Collab Team, 2020. Using a deep neural network and transfer learning to bridge scales for seismic phase picking. Geophys. Res. Lett. 47 (16), e2020GL088651.

Chen, Y., Huang, L., EGS Collab Team, et al., 2019. Optimal design of 3D borehole seismic arrays for microearthquake monitoring in anisotropic media during stimulations in the EGS collab project. Geothermics 79, 61–66.

Chi, B., Huang, L., Gao, K., Ajo-Franklin, J., Kneafsey, T.J., 2020. Anisotropic imaging of created fractures in EGS collab experiments using CASSM data. In: 45th Workshop on Geothermal Reservoir Engineering. p. 6.

Chitrala, Y., Moreno, C., Sondergeld, C., Rai, C., 2013. An experimental investigation into hydraulic fracture propagation under different applied stresses in tight sands using acoustic emissions. J. Pet. Sci. Eng. 108, 151–161.

Condon, K.J., Sone, H., Wang, H.F., 2020. Low static shear modulus along foliation and its influence on the elastic and strength anisotropy of poorman schist rocks, homestake mine, south dakota. Rock Mech. Rock Eng. 1–25.

Derode, B., Guglielmi, Y., De Barros, L., Cappa, F., 2015. Seismic responses to fluid pressure perturbations in a slipping fault. Geophys. Res. Lett. 42 (9), 3197–3203.

Dobson, P., Kneafsey, T., Morris, J., Singh, A., Zoback, M., Roggenthen, W., Doe, T., Neupane, G., Podgorney, R., Wang, H., et al., 2018. The EGS collab hydroshear experiment at the sanford underground research facility–siting criteria and evaluation of candidate sites. Geothermal Resour. Council Trans. 42, 708–723.

Duboeuf, L., De Barros, L., Cappa, F., Guglielmi, Y., Deschamps, A., Seguy, S., 2017. Aseismic motions drive a sparse seismicity during fluid injections into a fractured zone in a carbonate reservoir. J. Geophys. Res. Solid Earth 122 (10), 8285–8304.

Dusseault, M., McLennan, J., Shu, J., 2011. Massive multi-stage hydraulic fracturing for oil and gas recovery from low mobility reservoirs in China. Petroleum Drill. Techn. 39 (3), 6–16.

Eyre, T.S., van der Baan, M., 2015. Overview of moment-tensor inversion of microseismic events. Leading Edge 34 (8), 882–888.

Frash, L.P., Carey, J.W., Welch, N.J., et al., 2019a. EGS collab experiment 1 geomechanical and hydrological properties by triaxial direct shear. In: 44th Workshop on Geothermal Reservoir Engineering.

Frash, L.P., Fu, P., Morris, J., EGS Collab Team, et al., 2018. Fracture caging: Can we control the extent of a hydraulic fracture stimulated zone. In: Proceedings 43rd Workshop on Geothermal Reservoir Engineering, Stanford University. p. 8.

Frash, L.P., Hampton, J.C., Gutierrez, M.S., et al., 2020. Fracture caging to control induced seismicity with inspiration from the EGS collab project. In: Proceedings 45th Workshop on Geothermal Reservoir Engineering. p. 10.

Frash, L.P., Welch, N.J., Carey, J.W., The EGS Collab Team, 2019b. Geomechanical evaluation of natural shear fractures in the EGS collab experiment 1 test bed. In: ARMA US Rock Mechanics/Geomechanics Symposium. ARMA, pp. ARMA–2019.

Fu, P., Morris, J., Wu, H., Yang, X., 2018. Imaging hydraulic fracture extents and aperture using electrical resistivity tomography. Technical Report, Lawrence Livermore National Lab.(LLNL), Livermore, CA (United States).

Fu, P., Schoenball, M., Ajo-Franklin, J.B., Chai, C., Maceira, M., Morris, J.P., Wu, H., Knox, H., Schwering, P.C., White, M.D., et al., 2021. Close observation of hydraulic fracturing at EGS collab experiment 1: Fracture trajectory, microseismic interpretations, and the role of natural fractures. J. Geophys. Res. Solid Earth 126 (7), e2020JB020840.

Gao, K., Huang, L., Knox, H., Schwering, P., Hoots, C., Ajo-Franklin, J., Kneafsey, T., 2020. Anisotropic elastic properties of the first EGS collab testbed revealed from the campaign cross-borehole seismic data. In: Proceedings 45th Workshop on Geothermal Reservoir Engineering, Stanford University, SGPTR-216. Preprint, https://Pangea.Stanford.Edu/ERE/Db/GeoConf/Papers/SGW/2020/Gao1.Pdf. (Last Access: January 2022).

Gischig, V.S., Doetsch, J., Maurer, H., Krietsch, H., Amann, F., Evans, K.F., Nejati, M., Jalali, M., Valley, B., Obermann, A.C., et al., 2018. On the link between stress field and small-scale hydraulic fracture growth in anisotropic rock derived from microseismicity. Solid Earth 9 (1), 39–61.

Guglielmi, Y., Cappa, F., Avouac, J.-P., Henry, P., Elsworth, D., 2015a. Seismicity triggered by fluid injection–induced aseismic slip. Science 348 (6240), 1224–1226.

Guglielmi, Y., Cappa, F., Lançon, H., Janowczyk, J.B., Rutqvist, J., Tsang, C.-F., Wang, J., 2015b. ISRM suggested method for step-rate injection method for fracture in-situ properties (SIMFIP): Using a 3-components borehole deformation sensor. In: The ISRM Suggested Methods for Rock Characterization, Testing and Monitoring: 2007-2014. Springer, pp. 179–186.

Hardebeck, J.L., Shearer, P.M., 2002. A new method for determining first-motion focal mechanisms. Bull. Seismol. Soc. Am. 92 (6), 2264–2276.

Hardebeck, J.L., Shearer, P.M., 2003. Using S/P amplitude ratios to constrain the focal mechanisms of small earthquakes. Bull. Seismol. Soc. Am. 93 (6), 2434–2444.

Helnwein, P., 2001. Some remarks on the compressed matrix representation of symmetric second-order and fourth-order tensors. Comput. Methods Appl. Mech. Engrg. 190 (22–23), 2753–2770.

Hopp, C., Rodríguez Tribaldos, V., Schoenball, M., Guglielmi, Y., Ajo-Franklin, J.B., Chakravarty, A., Team, E., 2020. The birth of a hydraulic fracture: Evolution of strain, displacement, seismicity, and temperature as measured by a borehole monitoring network during fracture propagation. In: AGU Fall Meeting Abstracts, Vol. 2020. pp. MR019–0010.

Ishida, T., 2001. Acoustic emission monitoring of hydraulic fracturing in laboratory and field. Constr. Build. Mater. 15 (5–6), 283–295.

Ji, C., Wald, D.J., Helmberger, D.V., 2002. Source description of the 1999 hector mine, california, earthquake, part I: Wavelet domain inversion theory and resolution analysis. Bull. Seismol. Soc. Am. 92 (4), 1192–1207.

Johnson, T.C., Strickland, C.E., Knox, H., Thomle, J., Vermeul, V.R., Ulrich, C., Kneafsey, T.J., Blankenship, D.A., 2019. EGS Collab Project Electrical Resistivity Tomography Characterization and Monitoring. Technical Report., Pacific Northwest National Lab.(PNNL), Richland, WA (United States).

Kneafsey, T.J., Blankenship, D., Dobson, P.F., Morris, J.P., White, M.D., Fu, P., Schwering, P.C., Ajo-Franklin, J.B., Huang, L., Schoenball, M., et al., 2020. The EGS collab project: Learnings from experiment 1. In: Proceedings of the 45th Workshop on Geothermal Reservoir Engineering, Stanford, CA, USA. pp. 10–12.

Kneafsey, T., Dobson, P., Ajo-Franklin, J., Guglielmi, Y., Valladao, C., Blankenship, D., Schwering, P., Knox, H., White, M., Johnson, T., et al., 2019. EGS collab project: status, tests, and data. In: ARMA US Rock Mechanics/Geomechanics Symposium. ARMA, pp. ARMA–2019.

Kneafsey, T.J., Dobson, P., Blankenship, D., Morris, J., Knox, H., Schwering, P., White, M., Doe, T., Roggenthen, W., Mattson, E., et al., 2018. An overview of the EGS collab project: field validation of coupled process modeling of fracturing and fluid flow at the sanford underground research facility, lead, SD. In: 43rd Workshop on Geothermal Reservoir Engineering, Vol. 2018.

Kwiatek, G., Martínez-Garzón, P., Plenkers, K., Leonhardt, M., Zang, A., von Specht, S., Dresen, G., Bohnhoff, M., 2018. Insights into complex subdecimeter fracturing processes occurring during a water injection experiment at depth in äspö hard rock laboratory, Sweden. J. Geophys. Res. Solid Earth 123 (8), 6616–6635.

Linneman, D., Sprinkle, P., Knox, H.A., Strickland, C.E., Johnson, T.C., Ingraham, M.D., Knox, J., Young, B., Schwering, P., Grubelich, M.C., et al., 2019. Baseline characterization for change detection with joint inversion of ERT and campaign seismic data. In: American Geophysical Union, Fall Meeting.

Martínez-Garzón, P., Kwiatek, G., Bohnhoff, M., Dresen, G., 2017. Volumetric components in the earthquake source related to fluid injection and stress state. Geophys. Res. Lett. 44 (2), 800–809.

Martínez-Garzón, P., Kwiatek, G., Ickrath, M., Bohnhoff, M., 2014. MSATSI: A MATLAB package for stress inversion combining solid classic methodology, a new simplified user-handling, and a visualization tool. Seismol. Res. Lett. 85 (4), 896–904.

Mattson, E.D., Zhang, Y., Hawkins, A., Johnson, T., Ajo-Franklin, J., Neupane, G.H., Plummer, M.A., 2019. Preliminary Collab fracture characterization results from flow and tracer testing efforts. Technical Report, Idaho National Lab.(INL), Idaho Falls, ID (United States).

Oldenburg, C., Dobson, P., Wu, Y., Cook, P., Kneafsey, T., Nakagawa, S., Ulrich, C., Siler, D., Guglielmi, Y., Ajo-Franklin, J., et al., 2020. Hydraulic fracturing experiments at 1500 m depth in a deep mine: Highlights from the kISMET project. Technical Report, Lawrence Berkeley National Lab.(LBNL), Berkeley, CA (United States).

Schoenball, M., Ajo-Franklin, J.B., Blankenship, D., Chai, C., Chakravarty, A., Dobson, P., Hopp, C., Kneafsey, T., Knox, H.A., Maceira, M., et al., 2020. Creation of a mixed-mode fracture network at mesoscale through hydraulic fracturing and shear stimulation. J. Geophys. Res.Solid Earth 125 (12), e2020JB019807.

Schoenball, M., Ajo-Franklin, J., Robertson, M., Wood, T., Blankenship, D., Cook, P., Dobson, P., Guglielmi, Y., Fu, P., Kneafsey, T., et al., 2019a. EGS collab experiment 1: Microseismic monitoring. Technical Report, USDOE Geothermal Data Repository (United States); Lawrence Berkeley National Lab.(LBNL), Berkeley, CA (United States).

Schoenball, M., Guglielmi, Y., Ajo-Franklin, J.B., Cook, P.J., Dobson, P., Hopp, C., Kneafsey, T.J., Soom, F., Ulrich, C., 2021. In-situ observation of pre-, co-and post-seismic shear slip at 1.5 km depth.

Schoenball, M., Guglielmi, Y., Ajo-Franklin, J.B., Cook, P.J., Dobson, P.F., Kneafsey, T.J., Knox, H.A., Schwering, P., Soom, F., Ulrich, C., 2019b. Direct observation of co-seismic deformation at 1.5 km depth: The egs collab fracture stimulation test. In: AGU Fall Meeting Abstracts, Vol. 2019. pp. S21F–0574.

Šílenỳ, J., Hill, D.P., Eisner, L., Cornet, F.H., 2009. Non–double-couple mechanisms of microearthquakes induced by hydraulic fracturing. J. Geophys. Res. Solid Earth 114 (B8).

Vavryčuk, V., 2015. Moment tensor decompositions revisited. J. Seismol. 19, 231–252.

Vavryčuk, V., Adamová, P., Doubravová, J., Jakoubková, H., 2017. Moment tensor inversion based on the principal component analysis of waveforms: Method and application to microearthquakes in west bohemia, czech Republic. Seismol. Res. Lett. 88 (5), 1303–1315.

Virieux, J., Operto, S., 2009. An overview of full-waveform inversion in exploration geophysics. Geophysics 74 (6), WCC1–WCC26.

Wang, H., Lee, M., Doe, T., Haimson, B., Oldenburg, C., Dobson, P., 2017. In-situ stress measurement at 1550-meters depth at the kISMET test site in lead, SD. In: 51st US Rock Mechanics/Geomechanics Symposium. OnePetro.

Warpinski, N., 2014. A review of hydraulic-fracture induced microseismicity. In: ARMA US Rock Mechanics/Geomechanics Symposium. ARMA, pp. ARMA–2014.

Wu, H., Fu, P., Morris, J.P., Mattson, E.D., Neupane, G., Smith, M.M., Hawkins, A.J., Zhang, Y., Kneafsey, T., EGS Collab Team, et al., 2021. Characterization of flow and transport in a fracture network at the egs collab field experiment through stochastic modeling of tracer recovery. J. Hydrol. 593, 125888.

Ye, Z., Ghassemi, A., Kneafsey, T., 2020. Deformation, failure and permeability evolution of sealed fractures in EGS collab poorman schist. In: 45th Workshop on Geothermal Reservoir Engineering.

Zang, A., Stephansson, O., Stenberg, L., Plenkers, K., Specht, S., Milkereit, C., Schill, E., Kwiatek, G., Dresen, G., Zimmermann, G., et al., 2017. Hydraulic fracture monitoring in hard rock at 410 m depth with an advanced fluid-injection protocol and extensive sensor array. Geophys. J. Int. 208 (2), 790–813.

Zhou, Q., Oldenburg, C.M., Kneafsey, T.J., et al., 2018. Modeling transport of multiple tracers in hydraulic fractures at the EGS collab test site. In: Proceedings, 43rd Workshop on Geothermal Reservoir Engineering.

Zhu, L., Ben-Zion, Y., 2013. Parametrization of general seismic potency and moment tensors for source inversion of seismic waveform data. Geophys. J. Int. 194 (2), 839–843.

Zhu, L., Zhou, X., 2016. Seismic moment tensor inversion using 3D velocity model and its application to the 2013 lushan earthquake sequence. Phys. Chem. Earth A/B/C 95, 10–18.